

THE TUMULTUOUS LIVES OF GALACTIC DWARFS AND THE MISSING SATELLITES PROBLEM

ANDREY V. KRAVTSOV¹, OLEG Y. GNEDIN², ANATOLY A. KLYPIN³
Draft version January 17, 2022

ABSTRACT

Hierarchical Cold Dark Matter (CDM) models predict that Milky Way sized halos contain several hundred dense low-mass dark matter satellites (the substructure), an order of magnitude more than the number of observed satellites in the Local Group. If the CDM paradigm is correct, this prediction implies that the Milky Way and Andromeda are filled with numerous dark halos. To understand why these halos failed to form stars and become galaxies, we need to understand their history. We analyze the dynamical evolution of the substructure halos in a high-resolution cosmological simulation of Milky Way sized halos in the Λ CDM cosmology. We find that about 10% of the substructure halos with the present masses $\lesssim 10^8 - 10^9 M_\odot$ (circular velocities $V_m \lesssim 30$ km/s) had considerably larger masses and circular velocities when they formed at redshifts $z \gtrsim 2$. After the initial period of mass accretion in isolation, these objects experience dramatic mass loss due to tidal stripping. Our analysis shows that strong tidal interaction is often caused by actively merging massive neighboring halos, even before the satellites are accreted by their host halo. These results can explain how the smallest dwarf spheroidal galaxies of the Local Group were able to build up a sizable stellar mass in their seemingly shallow potential wells. We propose a new model in which all of the luminous dwarf spheroidals in the Local Group are descendants of the relatively massive ($\gtrsim 10^9 M_\odot$) high-redshift systems, in which the gas could cool efficiently by atomic line emission and which were not significantly affected by the extragalactic ultraviolet radiation. We present a simple galaxy formation model based on the trajectories extracted from the simulation, which accounts for the bursts of star formation after strong tidal shocks and the inefficiency of gas cooling in halos with virial temperatures $T_{\text{vir}} \lesssim 10^4$ K. Our model reproduces the abundance, spatial distribution, and morphological segregation of the observed Galactic satellites. The results are insensitive to the redshift of reionization.

Subject headings: cosmology: theory–galaxies: formation–galaxies: dwarf–galaxies: halos– halos: evolution– methods: numerical

1. INTRODUCTION

Semi-analytic models of galaxy formation (Kauffmann et al. 1993; Bullock et al. 2000; Somerville 2002; Benson et al. 2002) and numerical simulations (Klypin et al. 1999b; Moore et al. 1999a) have convincingly showed that the expected number of dark matter clumps around the galactic Milky Way (MW) sized halos exceeds the observed number of satellites by an order of magnitude. The discrepancy may indicate that the amplitude of the small-scale primordial density fluctuations is considerably lower than expected in the Cold Dark Matter (CDM) scenarios (e.g., Kamionkowski & Liddle 2000; Zentner & Bullock 2003) or that dark matter is self-interacting (Spergel & Steinhardt 2000). An alternative “astrophysical” interpretation is that the mismatch indicates that galaxy formation in dwarf halos is inefficient.

Several plausible physical processes may suppress gas accretion and star formation in dwarf dark matter (DM) halos. The cosmological UV background, which reionized the Universe at $z > 6$, heats the intergalactic gas and establishes a characteristic time-dependent minimum mass for halos that can accrete gas (e.g., Efstathiou 1992; Thoul & Weinberg 1996; Quinn et al. 1996; Navarro &

Steinmetz 1997; Gnedin & Hui 1998; Kitayama & Ikeuchi 2000; Gnedin 2000; Dijkstra et al. 2003). The gas in the low-mass halos may be photoevaporated after reionization (Barkana & Loeb 1999; Shaviv & Dekel 2003; Shapiro et al. 2003). In particular, Shaviv & Dekel (2003) recently argued that halos with circular velocities of up to ~ 30 km s⁻¹ can be photo-evaporated by the UV background. At the same time, the ionizing radiation may quickly dissociate molecular hydrogen, the only efficient coolant for low-metallicity gas in such halos, and prevent star formation before the gas is completely removed (e.g., Haiman et al. 1997).

The combined effect of these processes is likely to leave all DM halos with masses $\lesssim \text{few} \times 10^9 M_\odot$ dark. This is consistent with current observational constraints which indicate that halos with $M < 10^{10} M_\odot$ are virtually devoid of galaxies (van den Bosch et al. 2003). It is thus remarkable that the dynamical masses of some of the Local Group dwarfs are only $\sim 10^7 M_\odot$ (Mateo 1998). How could such galaxies form stars despite the suppressing processes listed above?

One possibility is that they manage to accrete a certain amount of gas before the Universe is reionized (Bullock et al. 2000) with the implicit assumption that this gas can be subsequently converted to stars. However, it is likely that gas cooling and star formation in such small systems is inefficient. For example, cosmological simulations with self-consistent treatment of H₂ chemistry and radiative transfer indicate that star formation is strongly suppressed in halos with masses $M \lesssim 5 \times 10^8 M_\odot$ at all redshifts, even before reionization (Chiu et al. 2001). In addi-

¹ Dept. of Astronomy and Astrophysics, Center for Cosmological Physics, The University of Chicago, Chicago, IL 60637; andrey@oddjob.uchicago.edu

² Space Telescope Science Institute, 3700 San Martin Drive, Baltimore, MD 21218; ogedin@stsci.edu

³ Astronomy Department, New Mexico State University, MSC 4500, P.O.Box 30001, Las Cruces, NM, 88003-8001; aklypin@nmsu.edu

tion, the galaxies may not be able to form sufficiently early to accrete the gas in the first place, if the power spectrum normalization is low or the Universe was reionized early, as indicated by the first-year *WMAP* results (Spergel et al. 2003; Kogut et al. 2003). An alternative proposal was recently suggested by Stoehr et al. (2002, 2003) and corroborated by Hayashi et al. (2003), who argued that the host halos of the low-luminosity dwarf spheroidal galaxies may be considerably more massive than previously thought. In this case, the large halo mass could allow an object to resist the suppressing effects of UV background.

In this paper we study the dynamical evolution of dwarf satellite halos around the Milky Way-sized hosts in self-consistent cosmological simulations. We show that the evolution of such objects is complex and often involves dramatic tidal stripping, interactions with other satellites, mass loss, and changes of internal structure. Most importantly, we find that some of the satellites that have small masses and circular velocities at the present, once were considerably more massive and could have plausibly formed stars in the past. We argue that the evolution of these objects may explain how the smallest dwarfs in the Local Group managed to form their stellar populations.

The paper is organized as follows. In § 2 we describe the details of the numerical simulation used in our analysis. In § 3 and § 4 we discuss the algorithm used to identify halos and the method used to construct their evolutionary tracks. In § 5 we present the main results on the dynamical evolution, abundance, and radial distribution of the dwarf dark matter halos. In § 6 we present a model for star formation in these systems and compare results to the observed abundance and spatial distribution of the Local Group dwarfs. We discuss the implications of our results and compare our model to the previous studies in §§ 7 and 8. Finally, in § 9 we summarize our findings and conclusions.

2. SIMULATION

We used the Adaptive Refinement Tree N -body code (ART, Kravtsov et al. 1997; Kravtsov 1999) to follow the evolution of three Milky Way-sized halos in the concordance Λ CDM cosmology: $(\Omega_m, \Omega_\Lambda, h, \sigma_8) = (0.3, 0.7, 0.7, 0.9)$. The simulation starts with a uniform 256^3 grid covering the entire computational box. This grid defines the lowest (zeroth) level of resolution. Higher force resolution is achieved in the regions corresponding to collapsing structures by recursive refining of all such regions using an adaptive refinement algorithm. Each cell can be refined or de-refined individually. The cells are refined if the particle mass contained within them exceeds a certain specified value. The grid is thus refined to follow the collapsing objects in a quasi-lagrangian fashion.

The galactic halos were simulated in the comoving box of $25h^{-1}$ Mpc; they were selected to reside in a well-defined filament at $z = 0$. Two halos are neighbors, located at $425h^{-1}$ kpc (i.e., ≈ 610 kpc $\sim 2R_{\text{vir}}$) from each other. The configuration of this pair thus resembles that of the Local Group. The third halo is isolated and is located ~ 2 Mpc away from the pair.

Multiple mass resolution technique was used to set up initial conditions. Namely, a lagrangian region corresponding to a sphere of radius equal to two virial radii around

TABLE 1. PROPERTIES OF THE HOST HALOS

Halo	M_{vir} ($h^{-1}M_\odot$)	R_{vir} (h^{-1} kpc)	V_m (km s^{-1})	Environment
G ₁	1.66×10^{12}	298	213	isolated
G ₂	1.24×10^{12}	278	199	pair
G ₃	1.19×10^{12}	281	183	pair

Note – R_{vir} is the virial radius corresponding to the average density of 180 times the mean density of the universe in h^{-1} kpc; $M_{\text{vir}} = M(< R_{\text{vir}})$ in $h^{-1}M_\odot$ (both radius and mass are given for $z = 0$); V_m is the maximum circular velocity.

each halo was re-sampled with the highest resolution particles of mass $m_p = 1.2 \times 10^6 h^{-1}M_\odot$, corresponding to 1024^3 particles in the box, at the initial redshift of the simulation ($z_i = 50$). The high mass resolution region was surrounded by layers of particles of increasing mass with a total of 5 particle species. Only regions containing highest resolution particles were adaptively refined and the threshold for refinement was set to correspond to the mass of the four highest resolution particles. The maximum of ten refinement levels was reached in the simulations corresponding to the peak formal spatial resolution of 150 comoving parsec. Each host halo is resolved with $\sim 10^6$ particles within its virial radius at $z = 0$.

From this point, we will refer to the isolated halo as G₁ and the halos in pair as G₂ and G₃. These halos are called B₁, C₁, and D₁, respectively, in Klypin et al. (2001) and we refer the reader to this paper for further details. The main properties of these three host halos, the virial mass, radius, and maximum circular velocity, are given in Table 1. We choose to define the virial radius (and the corresponding virial mass) as the radius encompassing the density of 180 times the mean density of the universe. For the commonly used overdensity of 340, the virial radii and masses for G₁, G₂, and G₃ are $R_{340} = 231, 212, \text{ and } 213h^{-1}$ kpc and $M_{340} = 1.45 \times 10^{12}, 1.13 \times 10^{12}, \text{ and } 1.14 \times 10^{12}h^{-1} M_\odot$, respectively. The masses are in the range of possible MW halo masses (Klypin et al. 2002).

Figure 1 shows the mass aggregation history of the three host halos. They have similar masses at the present but rather different evolutionary histories. In all cases, there is a period of very rapid mass assembly at $z \gtrsim 2 - 3$ followed by a relatively quiescent accretion at $z \lesssim 1.5$, the behavior typical of hierarchically forming halos (Wechsler et al. 2002). Host G₁ undergoes a spectacular multiple major merger at $z \approx 2$, which results in a dramatic mass increase on a dynamical time scale. Halos G₂ and G₃ increase their mass in a series of somewhat less spectacular major mergers which could be seen as mass jumps at $5 < z < 1$. All three systems accrete little mass and experience no major mergers at $z \lesssim 1$ (or lookback time of ≈ 8 Gyr) and thus could host a disk galaxy. Note, however, that halos G₁ and G₃ experience minor mergers during this period.

3. HALO IDENTIFICATION

In this study we use a variant of the Bound Density Maxima (BDM, Klypin et al. 1999a) halo finding algo-

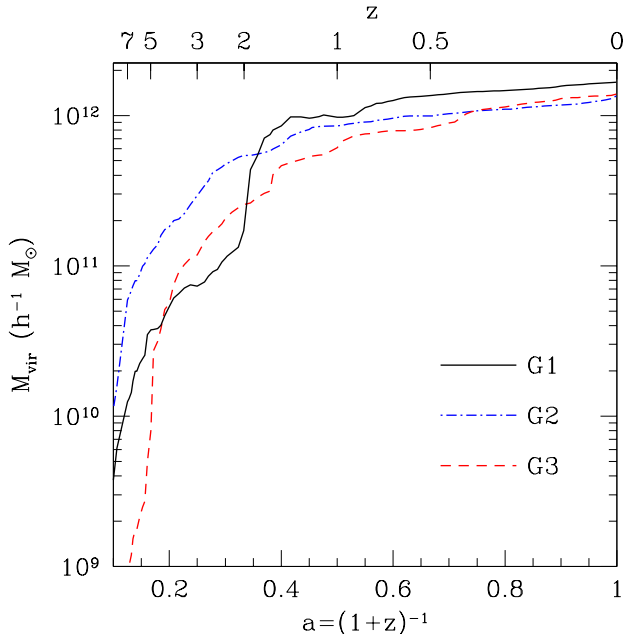


FIG. 1.— Mass aggregation histories for the three MW-size host halos analyzed in this study.

gorithm to identify halos both within (subhalos) and outside the host halos. Throughout this paper we will use the terms *subhalo*, *substructure*, and *satellite* interchangeably to indicate the distinct gravitationally self-bound halos located within the virial radius of a larger halo, which we call the *host*. The division is illustrated in Figure 2.

The BDM algorithm first finds positions of local maxima in the density field smoothed on a certain scale. Starting with the highest overdensity particle, we surround each potential density maximum by a sphere of radius $r_{\text{find}} = 10h^{-1}$ kpc and exclude all particles within this sphere from further search. The search radius is defined by the size of smallest systems we aim to identify. We verified that the results do not change if this radius is decreased by a factor of up to four. After all potential halo centers are identified, we analyze the density distribution and velocities of surrounding particles to test whether the center corresponds to a gravitationally bound clump. Specifically, we construct the density, circular velocity, and velocity dispersion profiles around each center and iteratively remove unbound particles (see Klypin et al. 1999a, for details). We then construct final profiles using only bound particles and use them to calculate such halo properties as the maximum circular velocity V_m , mass M , etc.

The virial radius is meaningless for the subhalos within a larger host as their outer layers are tidally stripped and the extent of the halo is truncated. The definition of the outer boundary of a subhalo and its mass are thus somewhat ambiguous. We adopt the truncation radius, r_t , at which the logarithmic slope of the density profile constructed from the bound particles becomes larger than -0.5 as we do not expect the density profile of the CDM halos to be flatter than this slope. Empirically, this definition roughly corresponds to the radius at which the density of the gravitationally bound particles is equal to the background host halo density, albeit with a large scatter. For some halos

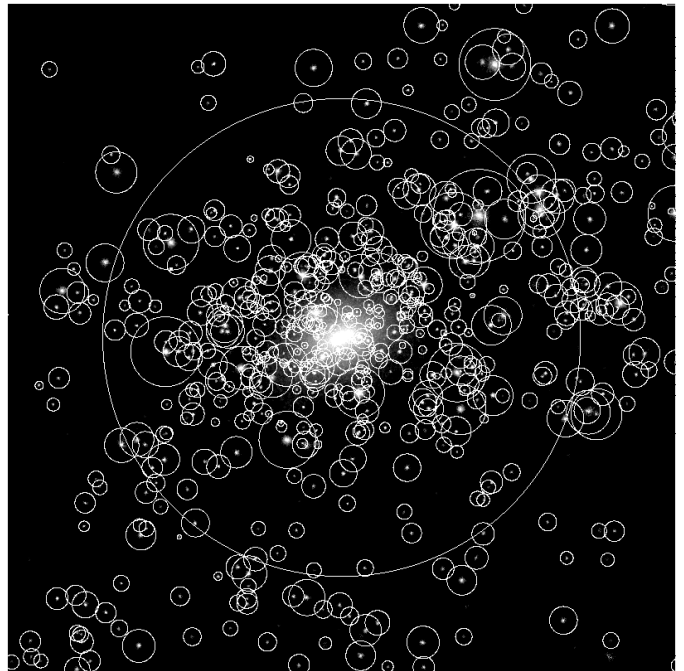


FIG. 2.— Distribution of dark matter particles (points) and dark matter halos (circles) identified by our halo finding algorithm centered on the isolated galactic halo at $z = 0$. The radius of the largest circle indicates the actual virial radius, R_{vir} , of the host halo ($R_{\text{vir}} = 298h^{-1}$ kpc); the radii of the other halos are the minimum between truncation radius r_t and R_{vir} . The particles are colored on a gray-scale logarithmic stretch according to their local density. The stretch is chosen to highlight the cores of the halos for clarity.

r_t is larger than their virial radius. In this case, we set $r_t = R_{\text{vir}}$. Throughout this paper, we will denote the minimum of the virial mass and mass within r_t , simply as M . For each halo we also construct the circular velocity profile $V_c(r) = \sqrt{GM(<r)}/r$ and compute the maximum circular velocity profile V_m .

Figure 2 shows the particle distribution in the halo G_1 at $z = 0$ along with the halos (circles) identified by the halo finder. The particles are color-coded on a gray scale according to the logarithm of their density to enhance visibility of substructure clumps. The radius of the largest circle indicates the actual virial radius, R_{vir} , of the host halo ($R_{\text{vir}} = 298h^{-1}$ kpc); the radii of the other halos are the minimum of the truncation radius r_t and R_{vir} . The figure demonstrates that the algorithm is efficient in identifying the substructure down to small masses.

4. CONSTRUCTING TRAJECTORIES

The halo finder described above was run at the 96 saved epochs between $z = 10$ and $z = 0$ with a typical spacing of $\sim 1 - 2 \times 10^8$ yr between outputs. For each epoch, the halo finder produced a halo catalog with positions, velocities, radii $r_h = \min(r_t, r_{\text{vir}})$, masses $m(<r_h)$, maximum of the circular velocity profile V_m and the radius at which the maximum occurs r_{max} . In addition, for each halo we save indices of all gravitationally-bound DM particles located within r_h .

This information is used to identify the progenitors of halos at successive epochs. Specifically, for a current epoch z_i , starting at $z = 0$, we search progenitors for each halo at several previous epochs z_{i-j} as follows. First, we select

a given fraction, f_{bound} , of the most bound particles of the halos at the epochs of consideration. We then compare the fraction of these particles that is common between all pairs of halos at successive epochs and assume that the halo with the highest common fraction is the progenitor. The trajectories used in this study were constructed using $f_{\text{bound}} = 0.25$. As the halo catalogs may miss some halos, especially near the completeness limit of the simulation, if the progenitor is not found at the previous epoch we need to search at the earlier epoch, etc. In particular, if a halo is located within the search radius r_{search} of some larger system it will not be identified by the halo finder. In constructing the trajectories we search for progenitors of a halo at z_i at epochs up to z_{i-4} . In the dominant majority of cases the progenitors are found at the previous epoch z_{i-1} . We experimented with other algorithms for progenitor identification and found the adopted prescription to be the most reliable and efficient.

5. RESULTS

5.1. Tidal stripping and dynamical evolution of satellite halos

Figure 3 shows three examples of the evolution of satellite halos. In the middle row of panels we plot the tidal force experienced by each object. The force was calculated both directly from the gravitational potential field computed in the simulation and analytically from the neighbor halo catalogs, as described in Appendix A. The Figure shows the trace of the tidal tensor, $F_{\text{tid}} = \sum_{\alpha} F_{\alpha\alpha}$, which is a good measure of the overall tidal field.

In all cases the tidal force experienced by the satellite coincides approximately with the time when the object is closest to the host, as expected. The Figure shows, for example, that at later epochs the tidal force calculated directly using the potential from the simulation can be well approximated by the analytical force from the host halo (see eq. A4). However, at earlier epochs (e.g., the highest peak in the left column) the force from the host underestimates the total tidal force. Thus, the overall tidal stripping is produced not only by the host halo but also by the massive neighbor halos, even *before the host is formed* (Gnedin 2003b).

The tidal heating by multiple halos is similar to “galaxy harassment” in clusters of galaxies (Moore et al. 1996, 1999b), except that it may occur when the halo is still isolated. As Figure 3 shows, the true force computed from the potential can be recovered if the analytical contributions of all neighboring halos are included. Their contribution is particularly important during major mergers of the host, when the centers of two or more massive halos are located in the close vicinity of each other and the satellite halos. Our analytic estimate describes the strong tidal peaks remarkably well, but becomes inaccurate for low (a few Gyr^{-2}) values of F_{tid} .

The amount of energy imparted to the halo depends on the square of the tidal force (eq. A6). Thus, by far the strongest tidal heating experienced by an object is during the highest tidal peaks. For the object in the left column of Figure 3, for example, most of the stripping and disruption is due to the tidal peak at $t \sim 4$ Gyr ($z \sim 1.5$). At this epoch, the host halo is not yet fully assembled and is undergoing a major merger with three other massive

halos. It is at this epoch, however, that the satellite experiences the most dramatic tidal mass loss. Subsequent tidal peaks result only in a relatively mild stripping. The object in the middle panel also suffers a dramatic mass loss at $t \sim 4 - 5$ Gyr. In this case, however, the efficient tidal stripping continues due to the later pericentric passages and associated peaks in the tidal force. Finally, the third satellite shown in the figure experiences only a relatively mild tidal stripping. This satellite orbits in the outer regions of the host and never reaches the central ≈ 60 kpc.

Note that the pericenter of the third satellite is larger at the late epochs compared to the pericenter at $t \approx 4$ Gyr. This is contrary to a naïve expectation that the pericenter should stay constant or decrease with time if dynamical friction is efficient. The real situation is clearly more complicated. The satellite can lose as well as gain the orbital energy. The latter can occur via a three-body interaction. Indeed, in examining individual trajectories we found cases where a satellite gains orbital energy via the “slingshot” acceleration — a classic three-body interaction.

Figure 3 demonstrates that some satellites with small maximum circular velocity and mass at $z = 0$ were substantially more massive during the early stages of their evolution. The mass of the object in the middle column is $\approx 10^{10} M_{\odot}$ and its circular velocity is $> 40 \text{ km s}^{-1}$ at $t = 4$ Gyr. At the present epoch, they are only $2 \times 10^8 M_{\odot}$ and 18 km s^{-1} , respectively. In the extreme cases we find changes of mass and V_{max} by a factor of 200 and 8, respectively (see Fig. 6).

At the same time, the object in the right column of Figure 3 has a considerably larger pericenter and experiences weaker tidal force by more than an order of magnitude. Consequently, its mass and circular velocity change little during the evolution. What is the relative frequency of such cases compared to the cases of dramatic mass loss? We address this question in the next section.

5.2. Internal structure evolution

Strong tidal forces experienced by orbiting halos lead to a substantial mass loss, preferentially at the outer radii. The changes in the inner regions are more subtle and occur at a slower rate but can nevertheless be significant (e.g., Klypin et al. 1999a; Hayashi et al. 2003; Stoehr et al. 2003; Kazantzidis et al. 2003). Figure 4 shows the maximum values of M and V_{max} reached by a satellite during its evolution vs. their present values. Most of the *surviving* satellites experience only mild evolution, less than a factor of two in V_{m} . Yet, there is a fair number of cases in which the evolution is significant. The average changes in M or V_{m} do not seem to depend on the halo mass.

Figure 5 shows the ratio of the mass at $z = 0$ to the maximum mass achieved by each satellite during its evolution vs. the ratio of the maximum circular velocities at these two epochs. The figure shows a strong correlation between the two ratios:

$$\frac{M^0}{M^{\text{max}}} = \left(\frac{V_{\text{m}}^0}{V_{\text{m}}^{\text{max}}} \right)^{\beta}, \quad \beta \approx 3 - 4, \quad (1)$$

where V_{m}^0 and M^0 are the values at the present and $V_{\text{m}}^{\text{max}}$ is the maximum circular velocity at the epoch when the halo reached the maximum mass, M^{max} . This correlation shows that the internal structure of satellites re-adjusts

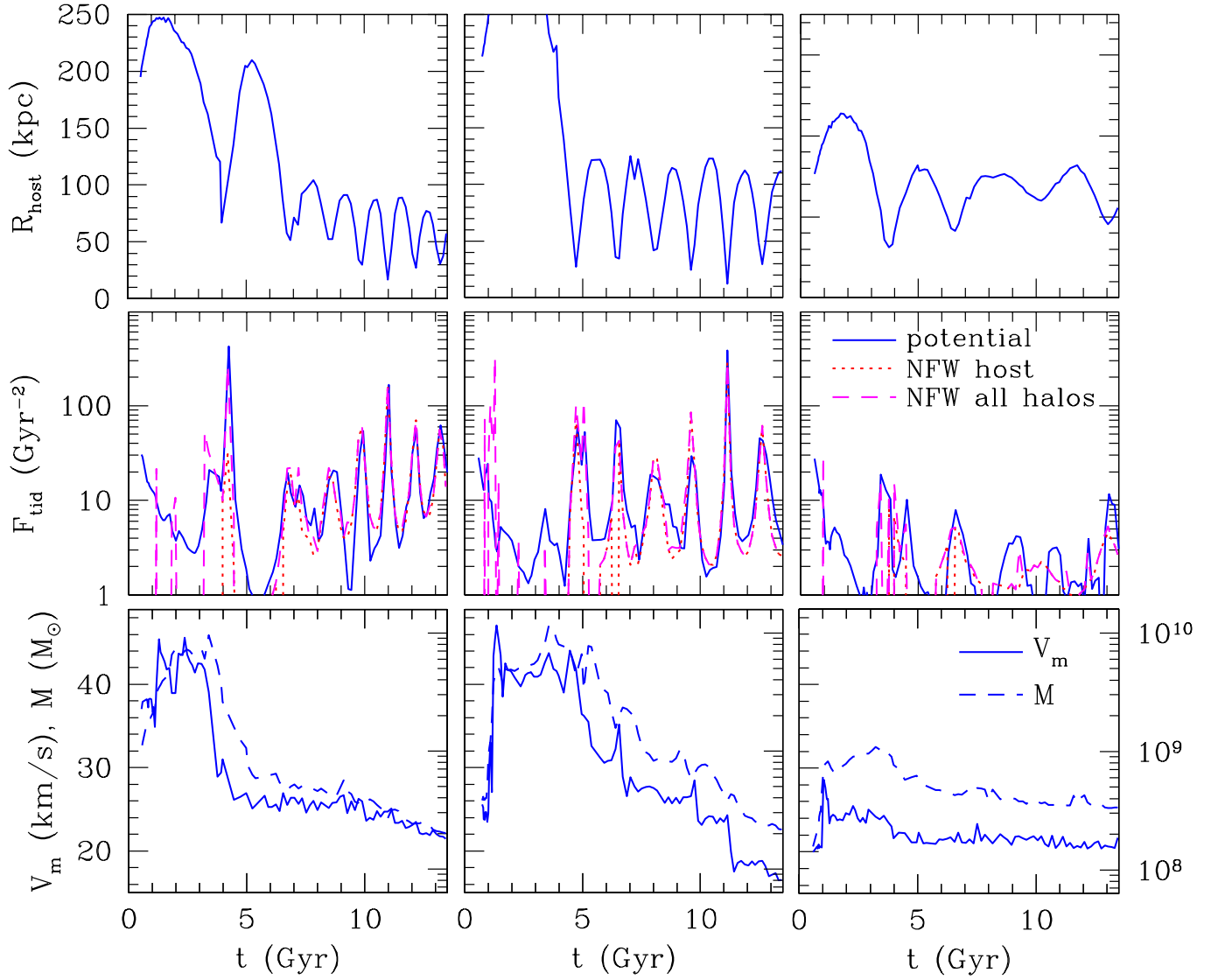


FIG. 3.— Three examples of the evolution of satellites of a MW-size host (different columns). *Top panels:* the proper distance between the satellite and the center of the host halo as a function of time. *Middle panels:* the tidal force experienced by the object, calculated directly from gravitational potential, is shown by the *solid line*. *Dotted line* shows the equivalent tidal force from the host halo with the host density profile approximated by an NFW model. *Dashed line* shows the contributions of all neighboring halos, including the host, with the density profiles of halos approximated by an NFW model with r_{\max} and V_m as measured in the simulation. See Appendix A for details on the tidal force calculation. *Bottom panels:* maximum circular velocity V_m (*solid lines*) and bound mass $m(< r_t)$ (*dashed lines*) as a function of time. The three objects show different types of evolution: dramatic early stripping with a relatively quiescent evolution afterward (left), continuous dramatic tidal stripping (middle), weak stripping and quiescent evolution (right).

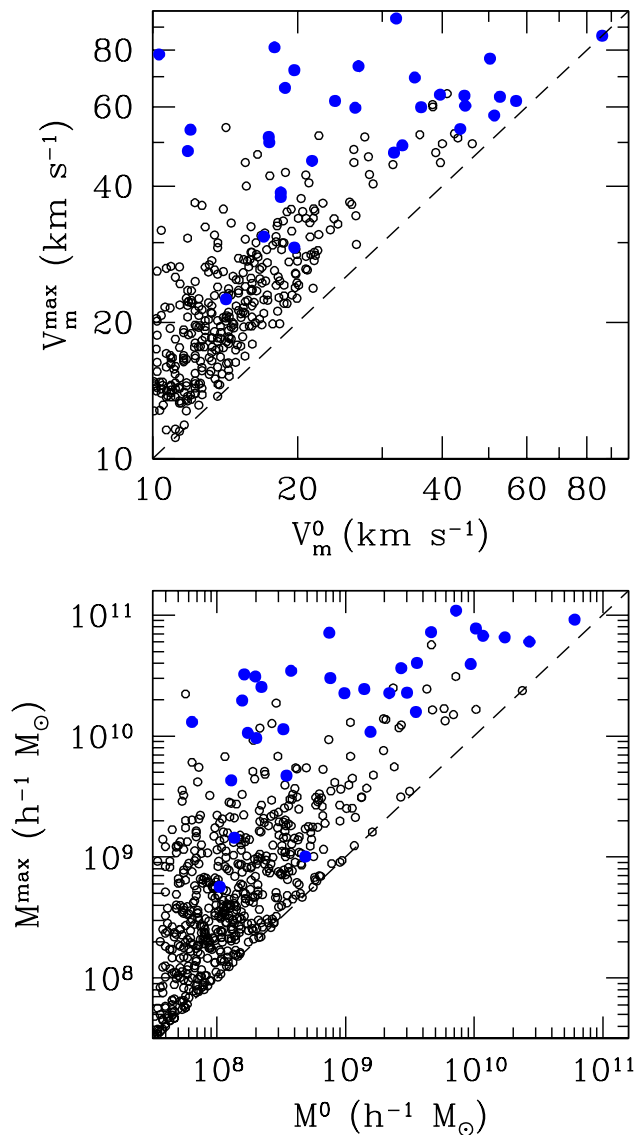


FIG. 4.— *Top panel:* the maximum circular velocity along the trajectory, V_m^{\max} , vs. the present-day value V_m^0 . *Bottom panel:* maximum mass along the trajectory vs. the present-day mass of a halo. The satellite halos shown are located within the virial radius of their respective host halo. The figure shows that many halos experience a dramatic decrease in their mass and circular velocity. The *solid circles* show the halos that host luminous galaxies in our model (see § 6).

as they lose mass due to tidal stripping. Note that the decrease of V_m indicates the decrease in density within the inner radius of $\approx 2.16r_s$, where r_s is the NFW scale radius. The adjustment is such that the virial correlation

$$M \propto V_m^\alpha, \quad \alpha \approx 3 - 4, \quad (2)$$

is approximately maintained at all times.

This can be seen in Figure 6, which shows the tracks of individual satellites in the $M - V_m$ plane. The satellites shown were selected from all three galactic hosts. We selected objects with large changes in mass to maximize the dynamic range. The figure shows that both during the periods of mass growth while evolving in isolation and the

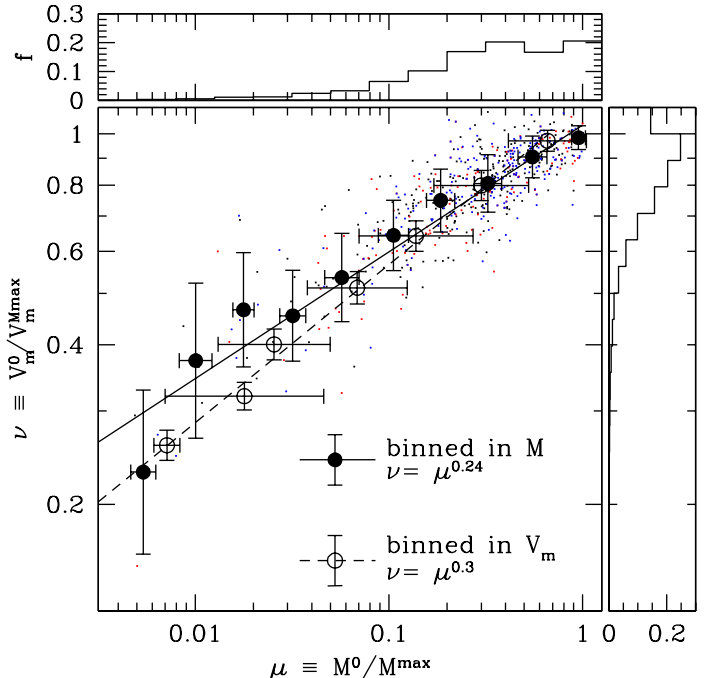


FIG. 5.— The ratio of the $z = 0$ mass to the maximum mass achieved by each satellite during its evolution vs. the ratio of the maximum circular velocities at these two epochs. The *dots* represent the ratios for individual halos. *Solid circles* show the average for the equally space logarithmic mass bins and *solid line* shows the power law weighted least square fit to these points. *Open circles* and the *dashed line* show the same for the binning in V_m . The histograms in the *top* and *right panels* show the fraction of the halos with a given mass and circular velocity ratio in logarithmic bins of size 0.2 and 0.05 for the mass and velocity ratios, respectively.

periods of mass decrease due to tidal stripping, halos approximately move up and down the power-law dependence of eq. (2). For instance, the track shown by in the top left panel starts at $M \approx 3 \times 10^8 h^{-1} M_\odot$ and $V_m \approx 30 \text{ km s}^{-1}$ at $z = 10$ and by the redshift $z = 2$ reaches the mass of $2 \times 10^{10} h^{-1} M_\odot$. In the ten billion years between $z = 2$ and $z = 0$, the halo loses 99.5% of the mass and its V_m decreases by a factor of eight. Yet, during the entire course of evolution the halo moves roughly along the $M \propto V_m^{3.3}$ line.

This result is in agreement with Hayashi et al. (2003), who found a correlation similar to that of eq. (1) using controlled N -body experiments to study the tidal stripping and internal structure of the NFW halos (see their Fig. 12). They note that the density at all radii changes in response to tidal shocking. The density decrease is greatest at large radii, so that the overall profile steepens while the normalization drops. The adjustment of the density profile leads to the decrease of both V_m and r_{\max} . We also find that r_{\max} of satellites in our simulations decrease systematically as they lose mass. A similar evolution of V_m as a function of mass loss is found in very high-resolution controlled simulations of Kazantzidis et al. (2003), which followed tidal stripping of an NFW satellite resolved with 10^7 particles (Stelios Kazantzidis, private communication).

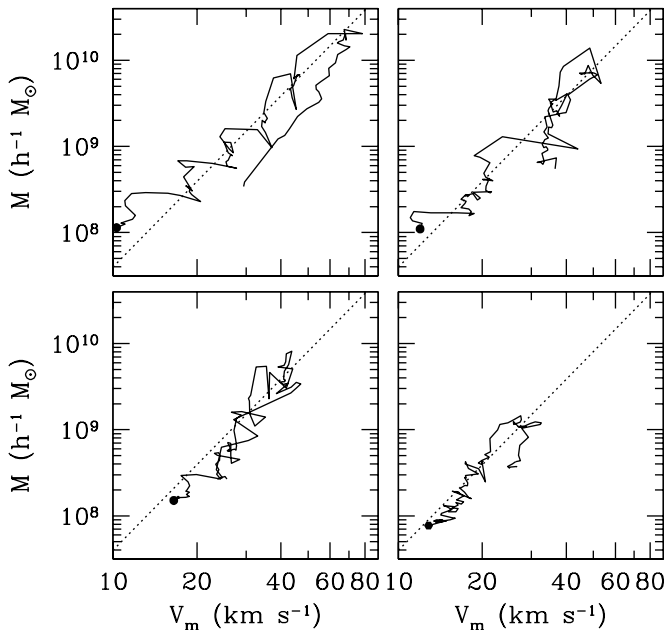


FIG. 6.— Trajectories (solid lines) of halos on the mass — maximum circular velocity plane for four halos found within the virial radius of all three galactic hosts at $z = 0$. We selected objects with large changes in mass to maximize the dynamic range and illustrate the effect. The solid circles mark the end ($z = 0$ epoch) of each trajectory. The figure shows that both during the periods of mass growth while evolving in isolation and the periods of mass decrease due to tidal stripping, halos approximately move up and down the virial dependence $M \propto V_m^\alpha$ with $\alpha \sim 3 - 5$; the dotted line corresponds to $\alpha = 3.3$.

5.3. Evolution of halos in the $M - V_m$ plane

In the previous section we showed that individual halos maintain $M \propto V_m^\alpha$ relation during their evolution. This explains why the same correlation between the mass and V_m holds for both subhalos and isolated halos (Avila-Reese et al. 1999; Bullock et al. 2001). We also find that the mass–circular velocity relations for the subhalos at $z = 0$ and for their progenitors at the epoch when the maximum mass was reached have similar amplitudes and slopes (≈ 3.3).

In this section we will consider the mechanism behind such behavior in more detail. We can interpret the observed evolution of mass and V_m for a given subhalo by dividing it in the following two stages: (1) mass growth while evolving in isolation, and (2) mass decrease due to tidal stripping after the halo is accreted by its host. The transition between the two stages typically occurs at $z \sim 2$ for the mass range of subhalos and hosts considered here.

We fit the slope α for the trajectories in the $M - V_m$ plane for all satellites separately in the two regimes. We fit only tracks of halos with $V_m > 15 \text{ km s}^{-1}$ at $z = 0$ and with at least 10 redshift outputs. In calculating the average slope, α_0 , and the dispersion of the sample, σ_α , we weigh α of each halo by the error of the fit. The isolated halos have the average slope $\alpha_0 = 4.7$, with the dispersion $\sigma_\alpha = 1.2$.

The truncated halos have $\alpha_0 = 2.9$ and $\sigma_\alpha = 1.2$. Thus the slopes in the two regimes seem to be somewhat different.

These different slopes can be linked to the different average densities of the dwarf halos in the two regimes. In the mass-growth stage, when the average density of the Universe is $\bar{\rho}(z) = \rho_0(1+z)^3$, the mass and velocity are given by the virial scaling relation $M_{\text{vir}} \propto V_{\text{vir}}^3(1+z)^{-3/2}$. Also, Bullock et al. (2001) showed that, as long as the NFW model is an adequate description of the halo profile, V_m and V_{vir} are related through the concentration parameter approximately as $V_m/V_{\text{vir}} \propto c_{\text{vir}}^{1/4}$. The median concentration itself varies with the mass and redshift as $c_{\text{vir}} \propto (1+z)^{-1}M_{\text{vir}}^{-0.13}$. Since all the variables scale as some power of $(1+z)$, it is natural to approximate the evolution of the mass and maximum velocity as $M_{\text{vir}} \propto (1+z)^{-q}$ and $V_m \propto (1+z)^{-p}$, with the above relations leading to $\frac{29}{32}q = 3p + \frac{3}{4}$. The slope $\alpha_0 = q/p = 4.7$ is achieved for $q = 2.8$ and $p = 0.6$, although the scatter in the value of α implies a corresponding scatter in the exponents q and p .

Note that the slope of the $M_{\text{vir}} - V_m$ relation is steeper than the virial $\alpha \approx 3$ because the virial parameters of isolated halos depend on the mean density of the Universe and that density is changing with redshift. The same zero-point of the relation can be maintained only if both M_{vir} and V_m are changing with time in a certain way, specified above.

During the second stage of evolution, the subhalo experiences tidal forces from the host and other halos, and its mass and extent are tidally truncated. The average density ρ_t within the truncation radius R_t is approximately constant along the orbit and is proportional to the background density of the host halo at the pericenter of subhalo’s orbit. The truncation radius scales with the truncated mass, M_t , as $R_t \propto (M_t/\rho_t)^{1/3}$, so that $M_t \propto V_t^3 \rho_t^{-1/2}$. The velocity $V_t \propto (M_t/R_t)^{1/2}$ is a good estimate for the peak velocity when the subhalo is severely truncated. If the background density is constant along the satellite trajectory, we obtain the following relation: $M_t \propto V_m^3$, in agreement with the average fit in this regime. Figure 6 shows that in this regime the power-law relation between M_t and V_m has a significant dispersion, which is due to the variation of ρ_t along the trajectory. Nevertheless, as long as the distance of closest approach to the host halo remains the same, the average relation is well maintained.

Thus, we expect the mass-velocity relation to be constrained by the two limiting slopes 3 and 5. The actual mass accretion and mass loss history may vary from halo to halo but the same $M - V_m$ relation is maintained throughout the evolution, with a transition from the initial slope $\alpha = 4.7$ for the isolated halos to the later slope $\alpha = 3$ for the tidally truncated halos.

5.4. Abundance and radial distribution of galactic satellites

Figure 7 shows the cumulative velocity functions (CVFs), the number of satellites with maximum circular velocity⁴

⁴ Note that uncertainty in the velocity anisotropy affects the conversion of the line-of-sight *rms* velocity of dSph galaxies to V_m . In the plot we assume an isotropic velocity distribution. Our re-analysis of numerical simulations of Gnedin (2003a) shows that tidal truncation and heating of galaxies leads to the preferential removal of radial

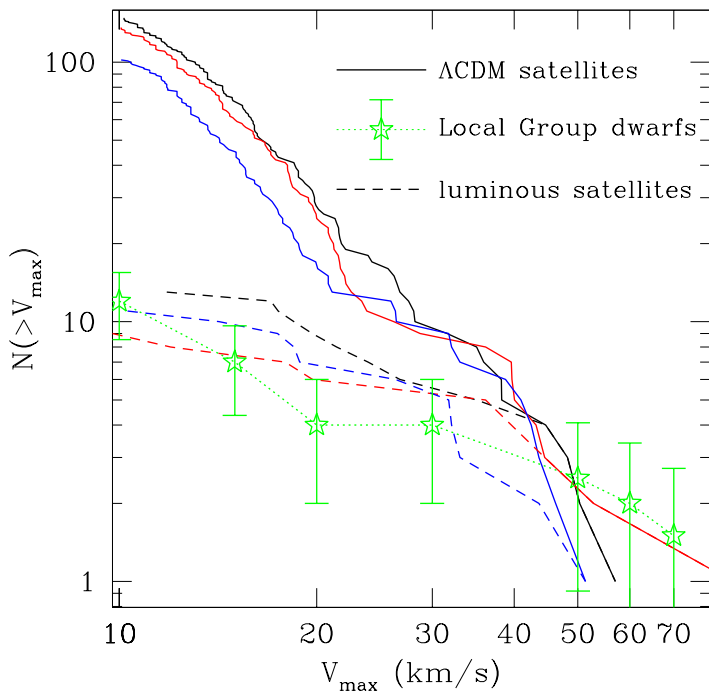


FIG. 7.— The cumulative velocity function of the dark matter satellites in the three galactic halos (*solid lines*) compared to the average cumulative velocity function of dwarf galaxies around the Milky Way and Andromeda galaxies (*stars*). For the objects in simulations V_{circ} is the maximum circular velocity, while for the Local Group galaxies it is either the circular velocity measured from rotation curve or from the line-of-sight velocity dispersion assuming isotropic velocities. Both observed and simulated objects are selected within the radius of $200h^{-1}$ kpc from the center of their host. The dashed lines show the velocity function for the luminous satellites in our model described in § 6. The minimum stellar mass of the luminous satellites for the three hosts ranges from $\approx 10^5 M_{\odot}$ to $\approx 10^6 M_{\odot}$, comparable to the observed range.

larger than a given value, for the objects located within $200h^{-1}$ kpc of their host halo. The figure compares the CVFs for the DM satellites and observed satellites of the MW and Andromeda⁵ and highlights the “missing satellite problem” (Kauffmann et al. 1993; Klypin et al. 1999b; Moore et al. 1999a): a large difference in the number of dwarf-size DM satellites in simulations and the observed number of dwarfs in the Local Group.

Figure 8 shows the normalized cumulative radial distribution of the DM satellites compared to the radial distribution of satellites around the Milky Way within the same radius. The Local Group data is from the compilation of Grebel et al. (2003). The figure clearly shows that the spatial distribution of dwarf galaxies around the Milky Way is more compact than the distribution of the DM popu-

orbits and the development of the tangentially-biased dispersion in the outer parts. A similar result has been found by Kazantzidis et al. (2004) and Moore et al. (2003). The solution of the Jeans equation for V_m is sensitive to the exact value of the anisotropy parameter (Zentner & Bullock 2003; Kazantzidis et al. 2003).

⁵ We use the circular velocities compiled by Klypin et al. (1999b) with updated values of circular velocity for the Large and Small Magellanic Clouds of $V_m = 50 \text{ km s}^{-1}$ and 60 km s^{-1} , respectively (van der Marel et al. 2002)

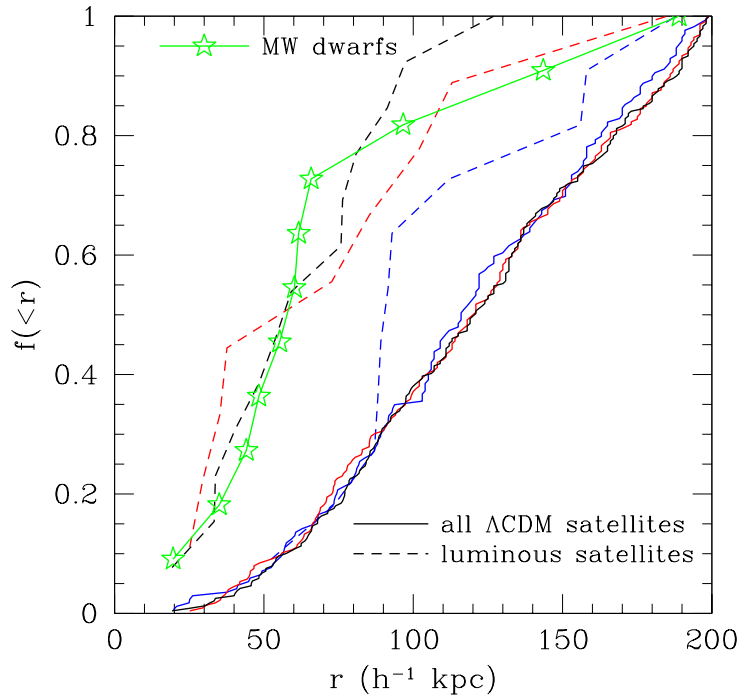


FIG. 8.— The fraction of satellites within a certain distance from the center of their host galaxy. The *solid lines* show distributions of the Λ CDM satellites in the three galactic halos, while the *connected stars* show the distribution of dwarf galaxies around the Milky Way. The figure shows that radial distribution of observed satellites is more compact than that of the overall population of dark matter satellites. The *dashed lines* show distributions for the luminous satellites in our model (§ 6). The population of luminous satellites is the same in this and previous figures.

lation. The median distance of observed satellites within $200h^{-1}$ kpc is $60h^{-1}$ kpc and $85h^{-1}$ kpc for the MW and M31, respectively. For the DM satellites the corresponding median distances are $116h^{-1}$ kpc, $121h^{-1}$ kpc, and $120h^{-1}$ kpc. Although the median for M31 satellites is smaller than that of the DM satellites, their radial distributions are formally consistent. However, the comparison with the M31 satellites is difficult at present because typical distance errors are $\sim 20 - 50$ kpc (and $\gtrsim 70$ kpc for some galaxies), comparable to the distance to the host.

For the MW satellites the typical distance errors are an order of magnitude smaller and the comparison is considerably more meaningful. The Kolmogorov-Smirnov (KS) test gives probability of $(6 - 8) \times 10^{-4}$ that the MW satellites are drawn from the same radial distribution as the DM satellites. This has also been pointed out recently by Taylor et al. (2003), who compared the spatial distribution of the MW satellites to results of their semi-analytic model of galaxy formation. Thus, in addition to the vastly different abundances of the observed and predicted satellites, there is a discrepancy in the radial distribution. Models that aim to reproduce the abundance of the LG satellites should therefore be able to reproduce the radial distribution as well.

6.1. Description of the Model

In order to gain insight into which halos might become luminous and which might not, we implement the following simple model of star formation. We use the standard assumption that the gas within the halos with the virial temperature $T_{\text{vir}} > 10^4$ K dissipates its energy via radiative cooling and forms a disk. We then apply the empirical Schmidt law to calculate the star formation rate in radial shells within the disk. The novel features of our model include: (i) use of mass accretion and stripping history of the dwarf halos extracted from simulation, (ii) effects of photoionizing extragalactic background using the filtering mass, (iii) effects of inefficient dissipation of the gas at $T_{\text{vir}} \lesssim 10^4$ K, and (iv) bursts of star formation due to strong tidal shocks. The details of the model are as follows.

(i) Using the mass assembly history (MAH) of a given satellite halo directly from the simulation, instead of a semi-analytic approach, we are able to trace the major merger events as well as the quiescent accretion of material. The halo mass increases in both regimes, but the star formation rates are very different. The use of simulation MAHs allows us to determine the accretion epoch of a satellite and follow its mass loss due to tidal stripping.

(ii) At each time output we calculate the accreted mass since the last time step, ΔM . We increase the total gas mass, M_g , in the satellite by the amount of cold gas in a single halo with the mass ΔM at that epoch: $\Delta M_g = f_g(M, z)\Delta M$. The fraction f_g takes into account the photoevaporation of baryons by extragalactic UV flux, using the filtering scale parametrization of Gnedin (2000) and taking the redshift of reionization to be $z_r = 7$. See Appendix B and equation (B3) for details. After the satellite enters the host halo, the accretion of new gas is halted and the disk scale length is fixed, although stars may continue to form from the remaining reservoir of cold gas.

We distribute the gas on a spherically symmetric grid of 50 radial shells, according to the surface density of an exponential disk: $\Sigma_g(r) = \Sigma_0 \exp(-r/r_d)$. We use the observed Schmidt law of star formation to estimate the star formation rate: $\dot{\Sigma}_* = 2.5 \times 10^{-4} (\Sigma_g/M_\odot \text{ pc}^{-2})^{1.4} M_\odot \text{ kpc}^{-2}$. Only the shells above the threshold $\Sigma_g > \Sigma_{\text{th}} \equiv 5 M_\odot \text{ pc}^{-2}$ form stars (Kennicutt 1998).

(iii) The scale length of the disk is determined by its angular momentum. For a rotationally-supported disk it is approximately $r_d = 2^{-1/2} \lambda r_{\text{vir}}$. The value of the angular momentum parameter is drawn randomly from the probability distribution

$$p(\lambda)d\lambda = \frac{1}{\sqrt{2\pi}\sigma_\lambda} e^{-\frac{(\ln \lambda/\bar{\lambda})^2}{2\sigma_\lambda^2}} \frac{d\lambda}{\lambda}, \quad (3)$$

with $\bar{\lambda} = 0.045$, $\sigma_\lambda = 0.56$, according to the latest measurement by Vitvitska et al. (2002). This is a key assumption of the semi-analytic models of galaxy formation.

However, small halos at high redshift could only cool by atomic hydrogen to about 10^4 K. If their virial temperature is only slightly above that equilibrium temperature, the gas would not be able to dissipate enough to reach a rotationally-supported state. Instead, its distribution would be more extended, which can have important implications for the star formation with a density threshold Σ_{th} . This effect is particularly important for dwarf halos.

We model the effect of inefficient dissipation by adopting the expansion factor that depends on the ratio of the virial temperature to the equilibrium temperature of 10^4 K. The gas would reach a Boltzmann distribution with the density $M/r^3 \propto \exp(-\Phi/kT)$, where Φ is the potential energy. Using the maximum circular velocity instead of the temperature and ignoring the slow variation of the potential, we can express the scale length of the gas as $r_d \propto \exp[c(V_4/V_m)^2]$, where c is a normalization factor and $V_4 = 16.7 \text{ km s}^{-1}$ is the virial velocity corresponding to $T_{\text{vir}} = 10^4$ K. We find that $c = 10$ is a best fit to the abundance and radial distribution of the Local Group galaxies (see §6.2). This scaling also provides a good description of the extent of the gas within halos in cosmological galaxy formation simulation described in Kravtsov & Gnedin (2003). Thus, we set the size of the gaseous disk at each time step to be

$$r_d = 2^{-1/2} \lambda r_{\text{vir}} \times e^{10(V_4/V_m)^2}. \quad (4)$$

Of course, r_d is not allowed to exceed the tidal radius of the halo, r_t . The gas in large halos with $V_m \gg V_4$ can cool efficiently and reach rotational support, but for small halos with $V_m \gtrsim V_4$ the extended distribution reduces the central concentration of the gas and hinders star formation.

(iv) Strong tidal forces, such as in the interacting or merging galaxies, may lead to a burst of star formation throughout the dwarf galaxy. The association of starbursts with strong peaks of the tidal force is motivated by theoretical models (Mayer et al. 2001a) and, to a certain extent, by observations (Zaritsky & Harris 2003). The latter suggest that the tidally-triggered star formation in the SMC can be accurately modeled as an instantaneous burst of star formation. Zaritsky & Harris (2003) find the best fit to their data when the star formation rate (SFR) varies as $r^{-4.6}$ with the distance to the Galaxy. The tidal interaction parameter, I_{tid} (see eq. [A7]), that reflects the integrated effect of a single tidal shock, is the most natural candidate for the parametrization of the tidally-triggered SFR. Ignoring the adiabatic correction, it varies with the distance to the perturber approximately as $I_{\text{tid}} \propto r^{-4}$ (but see the discussion in § 6.2).

We allow for the starburst mode of star formation, when the tidal interaction parameter exceeds a threshold value. After experimenting with different thresholds, we find that $I_{\text{tid,th}} = 4 \times 10^3 \text{ Gyr}^{-2}$ provides the best simultaneous fit to the velocity function and spatial distribution of the satellites. In all radial shells, a fraction $f_* = I_{\text{tid}}/4 \times 10^4 \text{ Gyr}^{-2}$ (with a maximum of $f_* = 0.5$) of the available gas is converted into stars instantaneously. The normalization of f_* is somewhat arbitrary and can be adjusted to fit the stellar masses of the satellites. Since the starburst changes drastically the distribution of gas in the galaxy, new infalling gas may have a very different angular momentum. Therefore, after each starburst we recalculate the value of λ according to eq. (3).

The external tidal force determines the truncation radius R_t of the satellite, outside which all stars and gas are lost. In a static gravitational field, the radius of the Roche lobe is set by the condition that the average density of matter in the satellite equals twice the local ambient density (for the isothermal sphere potential). In a dynamic situation of the satellite on an eccentric orbit experiencing tidal shocks, the truncation depends on the time-varying

tidal force. However, using N -body simulations of the dynamical evolution of galaxies in clusters, Gnedin (2003a) showed that the truncation radius can be accurately described by the same condition, $\rho_{\text{av}}(R_t) = 2 \rho_{\text{tid}}$, where the effective tidal density ρ_{tid} is related to the trace of the tidal tensor via

$$\rho_{\text{tid}} = 1.8 \times 10^{-5} \left(\frac{F_{\text{tid}}}{\text{Gyr}^{-2}} \right) M_{\odot} \text{pc}^{-3}. \quad (5)$$

The truncation occurs near the maximum of the tidal force along the orbit, usually at the perigalactic distance.

The knowledge of the external tidal force also allows us to estimate the tidal heating of stars in the satellite. After each tidal shock, typically once per orbit, the velocity dispersion of stars in each radial shell increases by the amount (Gnedin 2003b)

$$\Delta\sigma^2(r) = 0.32 \left(\frac{I_{\text{tid}}}{\text{Gyr}^{-2}} \right) \left(\frac{r}{\text{kpc}} \right)^2 \text{km}^2 \text{s}^{-2}. \quad (6)$$

The mass-weighted dispersion σ may serve as an indicator of the morphological type of the satellite. In §6.2, we adopt the ratio of the rotation velocity to the velocity dispersion, v_{rot}/σ , as a possible criterion. In practice, we compute v_{rot} as the circular velocity of the NFW halo at the radius enclosing all bound stars.

6.2. Results

We show the predictions of our model for the cumulative velocity function and radial distribution of luminous satellites by dashed lines in Figures 7 and 8. The model reproduces fairly well both observational statistics. The abundance of luminous satellites and the shape of the velocity function are in reasonable agreement with observations. The stellar masses of the satellites are in the range $10^5 \lesssim M_* \lesssim 10^{10} M_{\odot}$, similar to the observed range of stellar masses of the LG galaxies (e.g., Dekel & Woo 2003). As can be seen in Figure 4, all of the luminous systems in our model, including those that have masses and circular velocities of the smallest dwarfs, were relatively massive ($M \gtrsim 10^9 M_{\odot}$ and $V_m \gtrsim 30 \text{ km s}^{-1}$) at some point in their evolution.

In comparison to the observed velocity functions it is worth noting that the conversion between the line-of-sight stellar velocity dispersions and maximum circular velocity is somewhat uncertain (Stoehr et al. 2002; Zentner & Bullock 2003; Kazantzidis et al. 2003). Thus, at this point it is not worth trying to reproduce the observed function exactly.

The median distances of luminous satellites to their respective hosts are $59h^{-1} \text{ kpc}$, $91h^{-1} \text{ kpc}$, and $73h^{-1} \text{ kpc}$ for halos G₁, G₂, and G₃, respectively. This is close to the median values for the MW and M31 and lower than the median distance of the overall DM satellites ($\approx 120h^{-1} \text{ kpc}$, see § 5.4). The KS probability that the radial distribution of these luminous satellites is drawn from the same distribution as that of the MW are 97%, 1%, and 75% for the three hosts, respectively. Although there are apparent fluctuations due to the differences in the evolutionary histories of the three hosts, the luminous satellites in our model have a clear tendency to be more centrally concentrated than the overall DM satellite population.

On the other hand, tidally-triggered bursts of star formation are not limited to the central parts of the host halo.

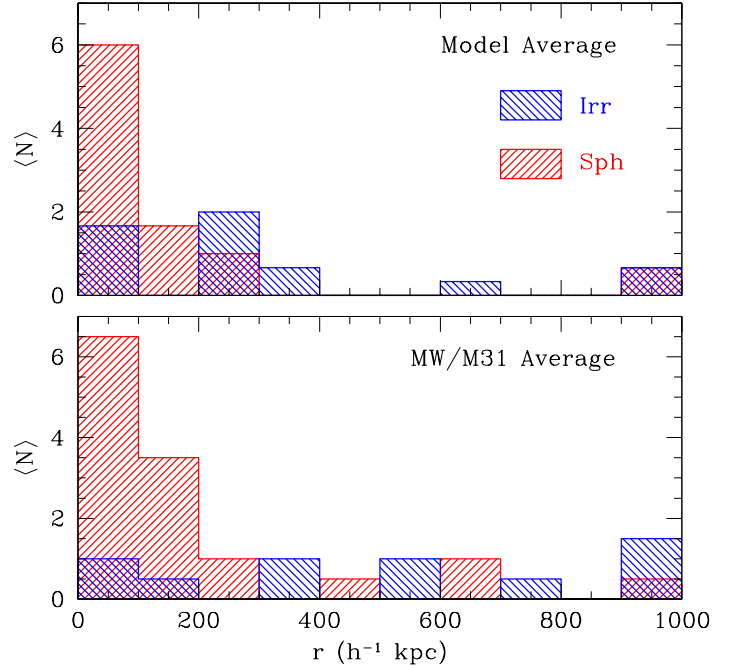


FIG. 9.— Morphological segregation of galaxies in the Local Group (lower panel) and in our model (upper panel). We divided the observed galaxies in two broad classes: Irr – all dwarf irregular galaxies, and Sph – all spheroidal systems, including dSph, dSph/dIrr, and dEs. The model result include all subhalos that formed stars and the division into irregular and spheroidal systems was done using the amount of heating experienced by each object, as explained in § 6.2. The model reproduces the observed morphological segregation: most spheroidal systems are located within $300h^{-1} \text{ kpc}$ of the host, while irregular systems are found at a wide range of radii.

In the isolated halo G₁, where the sample of satellites is not contaminated by the close proximity to another host, the tidal heating parameter I_{tid} scales with the present distance as $I_{\text{tid}} \propto r^a$, $a = -3.7 \pm 0.2$, for $r < 1 h^{-1} \text{ Mpc}$, where the quoted error is the standard deviation of the whole sample, not the error of the mean. This is consistent with the expected slope $a = -4$ (c.f. eq. [A6], ignoring the adiabatic correction). However, if we limit the sample to the halos of interest, i.e. only those capable of forming stars (with the maximum $V_m > V_4 = 16.7 \text{ km s}^{-1}$, the virial velocity corresponding to $T_{\text{vir}} = 10^4 \text{ K}$), then the slope is significantly shallower: $a = -1.8 \pm 0.2$. Furthermore, if we consider only the largest tidal parameters that might lead to starbursts ($I_{\text{tid}} > 10^3 \text{ Gyr}^{-2}$), then the distribution is almost independent of distance: $a = -0.3 \pm 0.1$. Thus, the current location of the satellite in the host galaxy gives very little indication whether it had tidal starbursts in the past.

We find a large variety of star formation histories for the luminous satellites. Most systems have a single initial burst lasting up to 2 Gyrs. For some this is the only starforming activity, while other have a constant SFR at $1 M_{\odot} \text{ yr}^{-1}$ up to $z = 0.7$ or bursty star formation continuing until $z = 0.2$. There are also objects that have only a single tidally-triggered burst at $z \sim 1$. The tendency is for more massive satellites to have more extended star formation. The median mass-weighted epoch of star formation

in halos with $V_m < 30 \text{ km s}^{-1}$ is between $t_{\text{med}} = 1 - 4 \text{ Gyr}$ cosmic time (corresponding redshifts $z = 5 - 1.7$), while the more massive halos have t_{med} up to 7 Gyr ($z = 0.7$).

Our simple model also predicts central stellar densities in a reasonable agreement with observations: roughly constant $\Sigma_* \sim 5 - 50 \text{ M}_\odot \text{ pc}^{-2}$ for $M_* < 10^9 \text{ M}_\odot$ and rising with the stellar mass as $\Sigma_* \sim M_*/(10^7 \text{ M}_\odot) \text{ M}_\odot \text{ pc}^{-2}$ for systems with $M_* > 10^9 \text{ M}_\odot$. The satellites located within 100 kpc of their host galaxy have typically higher central densities ($\gtrsim 50 \text{ M}_\odot \text{ pc}^{-2}$) than the more distant satellites.

The results listed above are valid for all dwarf satellite galaxies regardless of their evolutionary history. In addition, as discussed in the previous section, our model tracks the tidal heating of stars formed in each halo. We can therefore attempt a crude morphological classification of galaxies based on the amount of heating they experienced. This is motivated by the observations that dSph galaxies have low values of the ratio of rotation velocity to the random velocity dispersion, $v_{\text{rot}}/\sigma \lesssim 1$. The galaxies of transition type dIrr/dSph have $v_{\text{rot}}/\sigma \lesssim 2$ (see, e.g., Grebel et al. 2003, and references therein). Theoretical models of Mayer et al. (2001b,a) also indicate that the tidally-heated dSph-like remnants of low-surface brightness spiral galaxies have small v_{rot}/σ .

We use the circular velocity at the radius enclosing all of the stellar mass, v_c^{out} , as a proxy for v_{rot} . The rotation velocity will, in general, be smaller than the circular velocity because some of the kinetic energy is in the form of the random motions. Also, we account only for direct tidal heating and do not take into account tidally-induced heating via bar and bending instabilities. The exact value of v_{rot}/σ for our galaxies is thus somewhat uncertain as our σ may be regarded as lower limit. We experimented with several values for the classification threshold in the range $1 < v_c^{\text{out}}/\sigma < 3$, but the main trends are not sensitive to the specific choice in this interval. We chose the value of $v_c^{\text{out}}/\sigma = 3$ for the classification shown in Figure 9. For the observed galaxies, we combined dwarf spheroidal, transition type, and dwarf elliptical galaxies in one broad class of spheroidal systems, using Table 1 of Grebel et al. (2003). The figure shows that our model is consistent with the observed trend of morphological segregation. Most spheroidal systems are located within $300h^{-1} \text{ kpc}$ of the host, while irregular systems are found at a wide range of radii. The two model spheroidal systems at $\sim 1h^{-1} \text{ Mpc}$ have been part of a small group of galaxies and were tidally heated within this group before it was accreted by the host.

7. DISCUSSION

In the previous sections we presented the results of the dynamical evolution of galactic satellites in self-consistent cosmological simulations. One of the main findings is that the internal structure of the satellites responds to the changes of mass in a remarkably regular way. Namely, both during the periods of mass growth and tidal mass loss, the maximum circular velocity of a halo changes as $V_m \propto M^{1/\alpha}$. The slope α is $\sim 4 - 5$ when the mass grows and $\alpha \approx 3$ when the mass decreases due to tidal stripping. The latter result was also obtained by Hayashi et al. (2003) in their non-cosmological simulations of satellite evolution.

The overall evolution of subhalo population is such that their $M - V_m$ relation is similar to that of isolated halos

(with $\alpha \approx 3.3$). The fact that isolated halos and subhalos have similar mass-circular velocity relations may hint at why the fundamental plane of galaxies in clusters and the field are similar (Dressler et al. 1987; Djorgovski & Davis 1987; Mobasher et al. 1999; Bernardi et al. 2003) and why the scatter in the Tully-Fisher relation is so small (Kannappan et al. 2002).

The fact that the circular velocity decreases with decreasing mass means that the systems experiencing dramatic mass loss will experience a significant change in circular velocity. We find that about 10% of the subhalos with masses $< 10^8 - 10^9 \text{ M}_\odot$ or $V_m < 30 \text{ km s}^{-1}$ at $z = 0$ have considerably larger masses and circular velocities at earlier epochs. This may explain how such apparently small objects like Ursa Minor and Draco could have formed stars, given that the gas accretion is expected to be strongly suppressed by the UV background (e.g., Thoul & Weinberg 1996; Gnedin 2000). In our model, these systems were once sufficiently massive ($V_m \gtrsim 30 \text{ km s}^{-1}$) to accrete gas and form stars but the accretion was halted when they started to experience tidal mass loss.

After the accretion of new gas stops, these systems may continue to form stars in bursts as they are tidally stirred (e.g., Mayer et al. 2001b). Interestingly, we find that the strongest tidal interaction may occur even before halo is accreted by the host. Some satellites experience the strongest tidal force from multiple halos at early epochs in major mergers during the assembly of their host (see Fig. 3). Such mergers are frequent at early epochs, and we find that in general all satellites forming stars experience multiple bursts in the first $2 - 3 \text{ Gyrs}$ of their evolution. We present a simple model for star formation in dwarf halos and apply it to the evolutionary tracks extracted from the simulations. As shown in Figure 7, the model is successful in reproducing the abundance of luminous satellites around M31 and the Milky Way.

The spatial distribution of dwarfs around the Milky Way offers another independent challenge to any model of satellite evolution. Figure 8 shows that our model reproduces the observed distribution reasonably well. The distribution of luminous satellites is more compact than the overall population of subhalos because stars form only in objects that were sufficiently massive at high redshifts. Due to the strong mass- and redshift-dependence of spatial bias, such objects are considerably more clustered around the host than smaller halos that form at a wide range of redshifts. Correspondingly, we find that luminous objects were accreted by the host systematically earlier (by $\Delta z \sim 0.5 - 1$) than smaller mass dark subhalos.

One of the remarkable features of our model is that the results are not sensitive to the details of reionization history of the Universe. For example, all of the presented results are nearly intact if we change the assumed redshift of reionization from the fiducial value of $z_r = 7$ to $z_r = 15$ (see § B). The physical reason behind this insensitivity to reionization is the inefficiency of gas cooling and star formation in small mass ($T_{\text{vir}} \lesssim 10^4 \text{ K}$) systems. This is because gas in such systems cannot cool via hydrogen line emission and must rely on the inefficient H_2 cooling. Such redshift-independent suppression of gas cooling is observed in cosmological simulations of Chiu et al. (2001) and Kravtsov & Gnedin (2003). The important implication is

that properties of the population of galactic satellites are determined by the physics of galaxy formation rather than by the UV background and reionization.

Our results can qualitatively explain the morphological segregation of the Local Group galaxies (e.g., Grebel 2000). As shown in Figure 9, a simple division of model galaxies into irregular and spheroidal based on the amount of tidal heating they experienced during their evolution reproduces the main observed trend. Most spheroidal systems are located within $300h^{-1}$ kpc, while irregular galaxies are found almost uniformly at all distances. Therefore, our results support the scenario that spheroidal systems form via strong tidal heating (Mayer et al. 2001b,a). Note, however, that tidal heating is not restricted to the host. It can occur early on, before the host is assembled, within merging subgroups.

Interestingly, this explains a puzzling presence of the Cetus and Tucana dSph galaxies at the outskirts of the Local Group some 700 kpc and 1000 kpc from the nearest massive spiral (MW or M31). We also find $\sim 1-2$ galaxies with significant heating (the ratio of the rotational velocity to the velocity dispersion of $v_{\text{rot}}/\sigma < 1$) at distances ~ 1000 kpc from their hosts. The tidal heating of these systems occurred in small groups that are being accreted by the host at the current epoch (see also Gnedin 2003b, for a similar effect in clusters of galaxies). As the tidal force unbinds satellites from such accreting groups, isolated dSph galaxies may be found at large distances from the primary host.

Also, early tidal interaction, experienced for example by the system shown in the left column of Fig. 3, and subsequent interaction with other subhalos may lead to the increase of orbital energy and apocenter distance. This scenario would also explain presence of dSphs at large distances from the primary. The main point in both scenarios is that primary is not the only source of tides and the present-day environment is not necessarily indicative of a dwarf galaxy’s past.

One of the most interesting candidates for the “missing” dark halo is the population of compact high-velocity clouds (CHVCs) of neutral hydrogen (HI, e.g., Blitz et al. 1999; Braun & Burton 1999). This idea has recently been boosted by the detection of concentration of CHVCs near M31 (Thilker et al. 2003). It is thus interesting to consider the amount of gas associated with the subhalos that remain dark in our model. The cumulative gas mass function associated with dark halos is remarkably consistent for all three host halos: $N(> M_g) \approx 20(M_g/10^7 M_\odot)^{-0.7}$ for $10^6 < M_g \lesssim 10^8 M_\odot$ within $200h^{-1}$ kpc. Most of the gas mass is thus in most massive subhalos. The total mass of gas associated with such halos within $200h^{-1}$ kpc is $M_g^{\text{tot}} \approx 2 \times 10^9 M_\odot$, the number similar for all three hosts. If we assume that on the average about 10% of gas is neutral (Maloney & Putman 2003; Thilker et al. 2003), the total mass in neutral hydrogen is $M_{\text{HI}} \approx 2 \times 10^8 M_\odot$.

The predicted number of dark clouds with $M_g > 10^6 M_\odot$ is $\sim 50-100$. A fraction of the observed CHVCs can thus be associated with the small-mass DM halos. Within central 50 kpc, however, the number of halos with such gas masses is only $\sim 2-5$. We cannot therefore explain 25 CHVCs observed by Thilker et al. (2003) within this radius around M31. It is possible that simulations underpredict

the number of small-mass halos due to overmerging. To check this will require higher-resolution simulations. On the other hand, we did not take into account processes such as ram pressure stripping, which would further reduce the number of halos with gas. Another possibility is that most of the observed M31 CHVCs are gas clouds in tidal streams, such as the Magellanic Stream, and are not associated with distinct dark matter halos (Putman et al. 2003).

8. COMPARISON WITH PREVIOUS WORK

Possible astrophysical solutions⁶ to the “missing satellite problem” have been considered in the last several years. Here we discuss the main differences of our model and the models proposed in previous studies.

Bullock et al. (2000), Somerville (2002), and Benson et al. (2002) discussed the formation and evolution of dwarf galactic satellites using semi-analytic models of different degrees of sophistication. The conclusion reached by all these studies is that the extragalactic UV background can greatly suppress the gas accretion and star formation in the majority of low-mass ($V_m \lesssim 30 \text{ km s}^{-1}$) halos. A small fraction of the dwarf halos that harbors stellar systems was assumed to have formed (i.e., assembled significant fraction of their mass) before reionization, when the level of UV radiation was low. This is because in all of these studies the maximum circular velocity of subhalos was assumed to be constant as the mass is tidally stripped. There was thus a simple one-to-one mapping between the circular velocity observed at $z = 0$ and at the time of accretion. Our results show that this assumption is incorrect (see also Hayashi et al. 2003; Kazantzidis et al. 2003). Another key difference is that tidal mass loss in our model can occur before a halo is accreted by the host, as a result of interactions with other halos. These effects are not accounted for in any of the semi-analytic models.

The implicit assumption in the above models is that the small systems would be able to retain the accreted gas and form stars after reionization. This assumption was justified at the time, as the first calculations of photoevaporation of gas indicated that halos with $V_m \gtrsim 10 \text{ km s}^{-1}$ might retain their gas (Barkana & Loeb 1999). More recent calculations, however, show that the gas could be gradually removed from halos of up to $V_{\text{max}} \approx 30 \text{ km s}^{-1}$ (Shaviv & Dekel 2003). In light of this result, the previous models would not be able to explain the formation and properties of luminous dwarfs, as the star formation in small halos would be suppressed after reionization. It would thus be difficult to explain the more extended star formation histories derived for many dSph galaxies in the Local Group (Grebel 2000).

In our model, the small-mass dwarfs are identified with the halos that were relatively massive at high redshift and could retain the gas and form stars after reionization. The star formation histories of dwarfs are thus more extended, in better accord with observations. As noted in the previous section, our model is also insensitive to the epoch of reionization and can accommodate early reionization sug-

⁶ The solutions that invoke astrophysics of galaxy formation within the standard CDM framework rather than modifications of the properties of dark matter particles and/or the shape of the initial power spectrum.

gested by results of the *WMAP* satellite (Spergel et al. 2003).

Our model and all of the models discussed above are qualitatively different from the proposal of Stoehr et al. (2002, 2003). These authors argued that the maximum circular velocity of the Local Group dwarfs may be systematically underestimated because it is derived from the stellar velocity dispersion within radii considerably smaller than r_{\max} , the radius at which the maximum halo velocity, V_m is reached (see, however, Kazantzidis et al. 2003). Stoehr et al. (2002, see also Hayashi et al. (2003)) suggested that the luminous dwarfs may be harbored by the most massive satellites of the DM halos. This has an important physical implication: if the dwarfs indeed occupy twelve or so most massive halos, then there exists a certain mass scale below which galaxy formation is completely suppressed. If, on the other hand, the dwarf galaxies occupy satellites with a variety of masses ($\sim 10^7 - 10^{10} M_\odot$), one has to explain why some fraction of small halos managed to light up the stars, while most others did not.

If the idea of Stoehr et al. (2002) is correct, our results indicate that circular velocities of dwarf spheroidal halos should have been even larger (by a factor of two or more) than the values inferred from the current observations. This could make halos of some galaxies uncomfortably massive. For example, Stoehr et al. (2002) derive the maximum circular velocity for the Draco in the range $\sim 35 - 55 \text{ km s}^{-1}$. This implies the pre-accretion values of $V_{\max} \gtrsim 70 \text{ km s}^{-1}$ and the pre-accretion mass comparable to those of M32, NGC 205, and M33. The fact that luminosity of Draco is almost four orders of magnitude lower than luminosities of these galaxies would present a major puzzle.

In addition, the radial distribution of the most massive satellites should be consistent with the observed radial distribution of the MW satellites. We find that in our simulations the radial distribution of subhalos with largest V_m is between that of the luminous satellites and all DM satellites shown in Figure 8. In a study of a larger sample of cluster halos, De Lucia et al. (2003) find that the radial distribution of the most massive halos is even more extended than that of the smaller mass objects. A similar point was made recently by Taylor et al. (2003), who used semi-analytic models for subhalo population to show that the radial distribution of the most massive halos is more extended than that of the MW satellites at $\gtrsim 3\sigma$ level. A caveat to this argument is that the sample of Milky Way satellites may be incomplete at large distances and more faint dwarf galaxies will be discovered in the future (Willman et al. 2004).

9. CONCLUSIONS

We presented a study of the dynamical evolution of galactic satellites using self-consistent high-resolution cosmological simulations of three MW-sized halos. Our main results and conclusions are as follows.

- We find that $\approx 10\%$ of the substructure halos that have masses of $< 10^8 - 10^9 M_\odot$ at the present epoch, had considerably higher masses and circular velocities when they formed at $z > 2$. After the initial period of mass accretion, while these objects evolve

in isolation, they suffer dramatic mass loss due to tidal stripping by actively merging massive neighboring halos. Strong tidal interactions can occur even before the dwarfs are accreted by their primary host halos.

- The decrease in mass due to tidal stripping is accompanied by the decrease in the maximum circular velocity, such that the objects evolve along a $M - V_m^\alpha$ relation with $\alpha \approx 3 - 4$.
- These results indicate that some of the systems that have small masses and circular velocities at $z = 0$ could have had masses comparable to those of the SMC and LMC in the past. This can explain how the smallest dwarf spheroidal galaxies observed in the Local Group were able to build up sizable stellar masses in such shallow potential wells.
- We present a simple galaxy formation model based on the evolutionary tracks extracted from the simulations. The novel features of the model are the starburst mode of star formation after the strong peaks of the tidal force and accounting for the inefficient dissipation of gas in halos with $T_{\text{vir}} \lesssim 10^4 \text{ K}$. The model can successfully reproduce the circular velocity function, radial distribution, morphological segregation of the observed Milky Way satellites, and the basic properties of galactic dwarfs such as stellar masses and densities.

We would like to thank Nick Gnedin for providing us with the results of his filtering mass calculation in numerical form and for his hospitality at the University of Colorado at Boulder where this paper was completed. We are also grateful to Andrew Zentner for useful comments and Stelios Kazantzidis for communicating results of his calculations prior to publication. The simulations presented here were performed on the Origin2000 at the National Center for Supercomputing Applications (NCSA). This work was supported by the National Science Foundation under grant No. AST-0206216 and AST-0239759 to the University of Chicago. OYG is supported by the STScI Fellowship.

REFERENCES

- Avila-Reese, V., Firmani, C., Klypin, A., & Kravtsov, A. V. 1999, *MNRAS*, 310, 527
- Barkana, R. & Loeb, A. 1999, *ApJ*, 523, 54
- Benson, A. J., Frenk, C. S., Lacey, C. G., Baugh, C. M., & Cole, S. 2002, *MNRAS*, 333, 177
- Bernardi, M., Sheth, R. K., Annis, J., Burles, S., Eisenstein, D. J., Finkbeiner, D. P., Hogg, D. W., Lupton, R. H., Schlegel, D. J., SubbaRao, M., Bahcall, N. A., Blakeslee, J. P., Brinkmann, J., Castander, F. J., Connolly, A. J., Csabai, I., Doi, M., Fukugita, M., Frieman, J., Heckman, T., Hennessy, G. S., Ivezić, Ž., Knapp, G. R., Lamb, D. Q., McKay, T., Munn, J. A., Nichol, R., Okamura, S., Schneider, D. P., Thakar, A. R., & York, D. G. 2003, *AJ*, 125, 1866
- Blitz, L., Spergel, D. N., Teuben, P. J., Hartmann, D., & Burton, W. B. 1999, *ApJ*, 514, 818
- Braun, R. & Burton, W. B. 1999, *A&A*, 341, 437
- Bryan, G. L. & Norman, M. L. 1998, *ApJ*, 495, 80

Bullock, J. S., Kolatt, T. S., Sigad, Y., Somerville, R. S., Kravtsov, A. V., Klypin, A. A., Primack, J. R., & Dekel, A. 2001, MNRAS, 321, 559

Bullock, J. S., Kravtsov, A. V., & Weinberg, D. H. 2000, ApJ, 539, 517

Chiu, W. A., Gnedin, N. Y., & Ostriker, J. P. 2001, ApJ, 563, 21

De Lucia, G., Kauffmann, G., Springel, V., & White, S. D. M. 2003, MNRAS submitted, [astro-ph/0306205](#)

Dekel, A. & Woo, J. 2003, MNRAS, 344, 1131

Dijkstra, M., Haiman, Z., Rees, M. J., & Weinberg, D. H. 2003, ApJ submitted, [astro-ph/0308042](#)

Djorgovski, S. & Davis, M. 1987, ApJ, 313, 59

Dressler, A., Lynden-Bell, D., Burstein, D., Davies, R. L., Faber, S. M., Terlevich, R., & Wegner, G. 1987, ApJ, 313, 42

Efstathiou, G. 1992, MNRAS, 256, 43P

Gnedin, N. Y. 2000, ApJ, 542, 535

Gnedin, N. Y. & Hui, L. 1998, MNRAS, 296, 44

Gnedin, O. Y. 2003a, ApJ, 589, 752

—. 2003b, ApJ, 582, 141

Gnedin, O. Y., Hernquist, L., & Ostriker, J. P. 1999, ApJ, 514, 109

Gnedin, O. Y. & Ostriker, J. P. 1999, ApJ, 513, 626

Grebel, E. K. 2000, in ESA SP-445: Star Formation from the Small to the Large Scale, [astro-ph/0005296](#), 87

Grebel, E. K., Gallagher, J. S., & Harbeck, D. 2003, AJ, 125, 1926

Haiman, Z., Rees, M. J., & Loeb, A. 1997, ApJ, 476, 458

Hayashi, E., Navarro, J. F., Taylor, J. E., Stadel, J., & Quinn, T. 2003, ApJ, 584, 541

Kamionkowski, M. & Liddle, A. R. 2000, Physical Review Letters, 84, 4525

Kannappan, S. J., Fabricant, D. G., & Franx, M. 2002, AJ, 123, 2358

Kauffmann, G., White, S. D. M., & Guiderdoni, B. 1993, MNRAS, 264, 201

Kazantzidis, S., Magorrian, J., & Moore, B. 2004, ApJ, 601, 37

Kazantzidis, S., Mayer, L., Mastropietro, C., Diemand, J., Stadel, J., & Moore, B. 2003, ApJ submitted, [astro-ph/0312194](#)

Kennicutt, R. C. 1998, ApJ, 498, 541

Kitayama, T. & Ikeuchi, S. 2000, ApJ, 529, 615

Klypin, A., Gottlöber, S., Kravtsov, A. V., & Khokhlov, A. M. 1999a, ApJ, 516, 530

Klypin, A., Kravtsov, A. V., Bullock, J. S., & Primack, J. R. 2001, ApJ, 554, 903

Klypin, A., Kravtsov, A. V., Valenzuela, O., & Prada, F. 1999b, ApJ, 522, 82

Klypin, A., Zhao, H., & Somerville, R. S. 2002, ApJ, 573, 597

Kogut, A., Spergel, D. N., & Barnes, C. e. a. 2003, ApJ submitted, [astro-ph/0302213](#)

Kravtsov, A. & Gnedin, O. 2003, ApJ submitted, [astro-ph/0305199](#)

Kravtsov, A. V. 1999, Ph.D. Thesis

Kravtsov, A. V., Klypin, A. A., & Khokhlov, A. M. 1997, ApJS, 111, 73

Maloney, P. R. & Putman, M. E. 2003, ApJ, 589, 270

Mateo, M. L. 1998, ARA&A, 36, 435

Mayer, L., Governato, F., Colpi, M., Moore, B., Quinn, T., Wadsley, J., Stadel, J., & Lake, G. 2001a, ApJ, 559, 754

—. 2001b, ApJ, 547, L123

Mobasher, B., Guzman, R., Aragon-Salamanca, A., & Zepf, S. 1999, MNRAS, 304, 225

Moore, B., Ghigna, S., Governato, F., Lake, G., Quinn, T., Stadel, J., & Tozzi, P. 1999a, ApJ, 524, L19

Moore, B., Katz, N., Lake, G., Dressler, A., & Oemler, A. 1996, Nature, 379, 613

Moore, B., Kazantzidis, S., Diemand, J., & Stadel, J. 2003, MNRAS submitted, [astro-ph/0310660](#)

Moore, B., Lake, G., Quinn, T., & Stadel, J. 1999b, MNRAS, 304, 465

Navarro, J. F. & Steinmetz, M. 1997, ApJ, 478, 13

Putman, M. E., Staveley-Smith, L., Freeman, K. C., Gibson, B. K., & Barnes, D. G. 2003, ApJ, 586, 170

Quinn, T., Katz, N., & Efstathiou, G. 1996, MNRAS, 278, L49

Shapiro, P. R., Iliev, I. T., & Raga, A. C. 2003, MNRAS submitted, [astro-ph/0307266](#)

Shaviv, N. J. & Dekel, A. 2003, MNRAS submitted, [astro-ph/0305527](#)

Somerville, R. S. 2002, ApJ, 572, L23

Spergel, D. N. & Steinhardt, P. J. 2000, Physical Review Letters, 84, 3760

Spergel, D. N., Verde, L., & Peiris, H. V. e. a. 2003, ApJ submitted, [astro-ph/0302209](#)

Stoehr, F., White, S. D. M., Springel, V., Tormen, G., & Yoshida, N. 2003, MNRAS, 345, 1313

Stoehr, F., White, S. D. M., Tormen, G., & Springel, V. 2002, MNRAS, 335, L84

Taylor, J. E., Silk, J., & Babul, A. 2003, in IAU Symposium, [astro-ph/0312086](#)

Thilker, D., Braun, R., Walterbos, R., Corbelli, E., Lockman, F., Murphy, E., & Maddalena, R. 2003, ApJL submitted, [astro-ph/0311571](#)

Thou, A. A. & Weinberg, D. H. 1996, ApJ, 465, 608

van den Bosch, F. C., Yang, X., & Mo, H. J. 2003, MNRAS, 340, 771

van der Marel, R. P., Alves, D. R., Hardy, E., & Suntzeff, N. B. 2002, AJ, 124, 2639

Vitvitska, M., Klypin, A. A., Kravtsov, A. V., Wechsler, R. H., Primack, J. R., & Bullock, J. S. 2002, ApJ, 581, 799

Wechsler, R. H., Bullock, J. S., Primack, J. R., Kravtsov, A. V., & Dekel, A. 2002, ApJ, 568, 52

Willman, B., Governato, F., Dalcanton, J. J., Reed, D., & Quinn, T. 2004, MNRAS submitted ([astro-ph/0403001](#))

Zaritsky, D. & Harris, J. 2003, ApJ submitted, [astro-ph/0312127](#)

Zentner, A. R. & Bullock, J. S. 2003, ApJ, 598, 49

APPENDIX

CALCULATION OF THE TIDAL FORCE

In our analysis we use the external tidal force experienced by each satellite halo to estimate the strength of tidal interaction. We calculate the force both directly from the gravitational potential computed in the simulation and using an analytical approximation for the neighbor halos.

To compute the tidal force numerically from the local potential Φ , we estimate its second spatial derivative at the center-of-mass of the satellite:

$$F_{\alpha} \equiv - \left(\frac{d^2 \Phi}{dR_{\alpha} dR_{\beta}} \right)_0 r_{\beta} \equiv F_{\alpha\beta} r_{\beta}, \quad (\text{A1})$$

where \mathbf{r} is the radius-vector in the satellite reference frame and \mathbf{R} is the radius-vector in the perturber reference frame. The potential Φ is calculated on the original refinement grid using the ART gravity solver. In the calculation of the potential, we subtract the self contribution of the halo and consider only the external tidal potential.

In a study of galaxy interactions in clusters of galaxies, Gnedin (2003b) used the Savitzky-Golay smoothing filter to interpolate the potential on a plane and calculate its derivatives from a smooth polynomial function. We employ a similar scheme but with the adaptive 4-th order interpolating polynomials in each of the three orthogonal planes around the satellite center of mass:

$$P_4(x, y) = \sum_{k,l=0}^4 c_{kl} x^k y^l \quad (\text{A2})$$

and the same for the xz and yz planes. The 4-th order expansion ensures a smooth second derivative of the potential. In each of the planes we extract a $n \times n$ subgrid centered on the original grid point, nearest to the satellite center. In order to obtain a uniform accuracy of the tidal force for satellites of different sizes, we choose the size of the subgrid cells to be closest to 1/4 of the satellite's tidal radius. The coefficients c_{kl} are calculated by minimizing χ^2 deviation

$$\chi^2 = \sum_{i,j=1}^n [P_4(x_i, y_j) - \Phi(x_i, y_j)]^2 \quad (\text{A3})$$

using the CERN Program Library routine MINUIT⁷. We have experimented with $n = 16, 32,$ and 64 and found that $n = 64$ provides the most accurate derivatives, as tested on the analytical NFW models. The tidal tensor components $F_{\alpha\beta}$ are then calculated by analytical differentiation of equation (A2).

⁷ <http://wwwasdoc.web.cern.ch/wwwasdoc/minuit/>

We compare the real tidal force due to the overall mass distribution in the simulation with the contributions of all neighboring halos, including the host halo. We model the halos with an NFW density profile and take their mass M_{vir} and virial radius r_{vir} directly from the halo catalogs generated by the halo finder (see § 3). We determine the scale radius of the NFW model for the satellite halos from the position of the maximum circular velocity, $r_s = r_{\text{max}}/2.16$. For the host halo, we use the parametrization $c_{\text{nfw}} \equiv r_{\text{vir}}/r_s = 16 a^{3/2}$, which is a best fit to the density profile of the analyzed host halos. The analytical tidal force in the reference frame of the satellite is then readily calculated using eq. (5) of Gnedin et al. (1999):

$$\mathbf{F}(\mathbf{r}) = \frac{GM(R)}{R^3} [(3 - \dot{\mu})(\mathbf{n} \cdot \mathbf{r}) - \mathbf{r}] \quad (\text{A4})$$

where \mathbf{r} is the radius-vector within the satellite, R is the distance to the perturber, $\mathbf{n} \equiv \mathbf{R}/R$, $\dot{\mu} \equiv d \ln M/d \ln R$, and $M(R)$ is the enclosed mass of the NFW model:

$$M(R) = M_{\text{vir}} \frac{\ln(1 + R/r_s) - 1 + (1 + R/r_s)^{-1}}{\ln(1 + c_{\text{nfw}}) - 1 + (1 + c_{\text{nfw}})^{-1}}. \quad (\text{A5})$$

Figure 3 shows that the approximate tidal force calculated in this manner is quite accurate, especially near the maximum of the tidal force.

Although the tidal force along the satellite trajectory varies rapidly with time, most of the tidal heating of stars and dark matter particles occurs near the strong peaks of the tidal force. Each of these tidal peaks can be considered as an independent tidal shock (Gnedin & Ostriker 1999; Gnedin 2003b). The amount of tidal heating, such as the increase of the velocity dispersion, is proportional to the integral over the peak of tidal force:

$$I_{\text{tid}}(t_n) \equiv \sum_{\alpha, \beta} \left(\int F_{\alpha\beta} dt \right)_n^2 \left(1 + \frac{\tau_n^2}{t_{\text{dyn}}^2} \right)^{-3/2}, \quad (\text{A6})$$

where the sum extends over all components of the tidal tensor, $\alpha, \beta = \{x, y, z\}$. The last factor is the correction for the conservation of adiabatic invariants of stellar orbits during the tidal shock (c.f., Gnedin & Ostriker 1999). Here τ_n is the effective duration of peak n at time t_n , and t_{dyn} is the dynamical time of the satellite. We take $t_{\text{dyn}} = 2\pi r_{1/2}/v_{\text{rot}}$, where $r_{1/2}$ is the half-mass radius of the stellar disk and v_{rot} is the circular velocity of the appropriate NFW model at $r_{1/2}$. The cumulative tidal heating parameter is the sum over all tidal peaks:

$$I_{\text{tid}} = \sum_n I_{\text{tid}}(t_n). \quad (\text{A7})$$

This parameter determines the increase of the velocity dispersion of stars (eq. [6]) in our model of dwarf galaxy formation (§6).

FILTERING MASS SCALE

We estimate the suppression of gas accretion due to the extragalactic UV background using the filtering mass scale, derived by Gnedin (2000). He defined M_{F} as the mass of the halo which would lose half of the baryons, compared to the universal baryon fraction. This *filtering mass* relates to the Jeans mass of the intergalactic gas integrated over the cosmic history (eq. [6] in Gnedin 2000):

$$M_{\text{F}}(a) = M_{\text{J0}} f(a)^{3/2}, \quad (\text{B1})$$

$$f(a) = \frac{3}{a} \int_0^a x T_4(x) \left[1 - \left(\frac{x}{a} \right)^{1/2} \right] dx$$

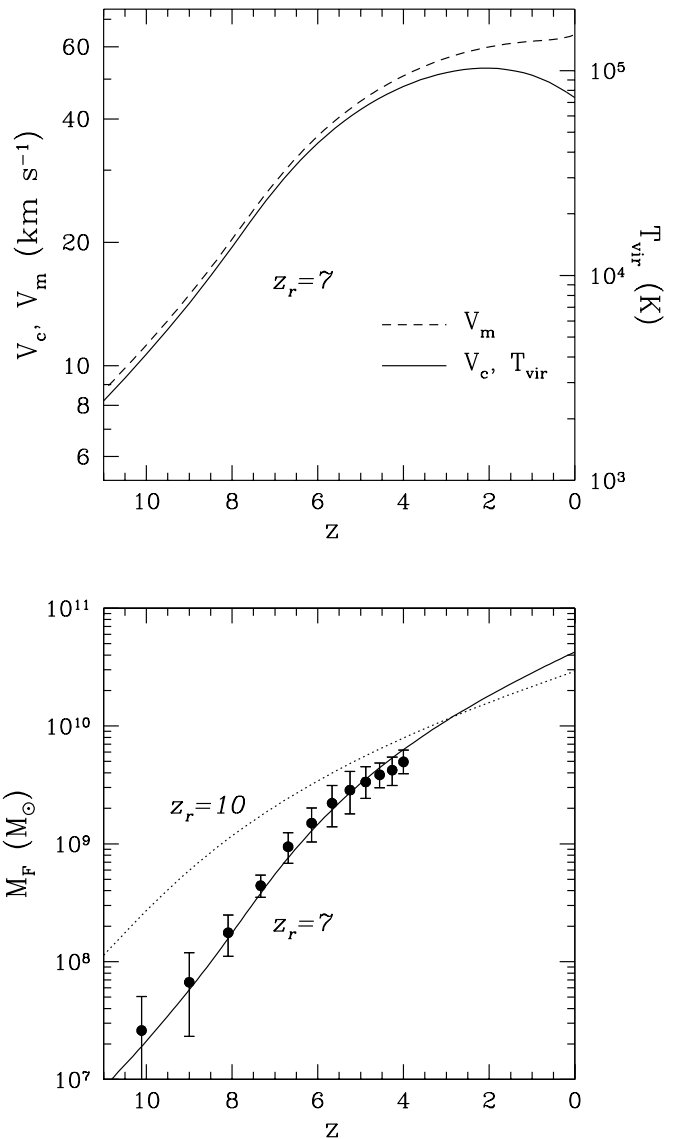


FIG. B10.— *Top panel*: filtering virial circular velocity (V_c) and virial temperature (axes are chosen such that the two solid lines coincide), and maximum circular velocity (V_m , dashed line). *Bottom panel*: filtering mass. Data points with error-bars show the simulation results of Gnedin (2000). Solid lines are for the standard epoch of reionization: $z_r = 7$, $z_o = 8$. For comparison, the dotted line in the bottom panel shows the case of earlier reionization with $z_r = 10$, $z_o = 11$.

where $M_{\text{J0}} = 2.5 \times 10^{11} h^{-1} \Omega_0^{-1/2} \mu^{-3/2} M_{\odot}$, $\mu \approx 0.59$ is the mean molecular weight of the fully ionized gas, and the integration extends over the expansion factor, a . The temperature of the cosmic gas T_4 is expressed in units of 10^4 K for convenience.

Here we propose an analytical fit to the results of Gnedin (2000), assuming a simple dependence of the temperature on the expansion factor: $T_4(a) = (a/a_o)^\alpha$ for $a \leq a_o$, $T_4(a) = 1$ for $a_o \leq a \leq a_r$, and $T_4(a) = (a/a_r)^{-1}$ for $a \geq a_r$.

These three distinct stages can be clearly seen on Fig. 1 of Gnedin (2000). They correspond, to the 1) epoch before the first HII regions form, $z > z_o$, 2) the epoch of

the overlap of multiple HII regions, $z_r < z < z_o$, and 3) the epoch of complete reionization, $z < z_r$. In the first stage, before redshift $z_o \equiv 1/a_o - 1 \approx 8$, the temperature is rising as the newly-formed stars ionize their neighboring regions. The parameter α controls the rate of growth of the extragalactic UV flux; we find $\alpha = 6$ to be the best fit. During the overlap stage, between redshifts z_o and $z_r \equiv 1/a_r - 1 \approx 7$, the temperature is kept constant at roughly 10^4 K as the cosmic HII regions overlap. After the universe is fully ionized, at redshifts below z_r , the temperature falls adiabatically with the cosmic expansion.

With these analytical expressions for $T_4(a)$, we integrate equation (B1) analytically:

$$f(a) = \frac{3a}{(2 + \alpha)(5 + 2\alpha)} \left(\frac{a}{a_o} \right)^\alpha, \quad a \leq a_o \quad (\text{B2})$$

$$f(a) = \frac{3}{a} \left\{ a_o^2 \left[\frac{1}{2 + \alpha} - \frac{2(a/a_o)^{-1/2}}{5 + 2\alpha} \right] + \frac{a^2}{10} - \frac{a_o^2}{10} \left[5 - 4(a/a_o)^{-1/2} \right] \right\}, \quad a_o \leq a \leq a_r$$

$$f(a) = \frac{3}{a} \left\{ a_o^2 \left[\frac{1}{2 + \alpha} - \frac{2(a/a_o)^{-1/2}}{5 + 2\alpha} \right] + \frac{a_r^2}{10} \left[5 - 4(a/a_r)^{-1/2} \right] - \frac{a_o^2}{10} \left[5 - 4(a/a_o)^{-1/2} \right] + \frac{aa_r}{3} - \frac{a_r^2}{3} \left[3 - 2(a/a_r)^{-1/2} \right] \right\}, \quad a \geq a_r.$$

The virial circular velocity of the halo is $V_c^3 = GMH(z)(\Delta_{\text{vir}}/2)^{1/2}$, where $H(z) = H(0)[\Omega_0(1 + z)^3 + \Omega_\Lambda]^{1/2}$ is the Hubble constant, and Δ_{vir} is the virial overdensity with respect to the critical density, parametrized by Bryan & Norman (1998) as $\Delta_{\text{vir}}(z) = 18\pi^2 + 82x - 39x^2$, $x \equiv \Omega(z) - 1$. The virial temperature is $T_{\text{vir}} = 36(V_c/\text{km s}^{-1})^2$ K.

Our analytical fit is convenient for accurate modeling of the photoheating effect in semi-analytical models of galaxy formation. Its versatile form, with two parameters z_o and z_r , allows a simple recalculation of the filtering mass for a different redshift of reionization than was assumed in the simulation of Gnedin (2000). It can also be easily adapted to describe two epochs of reionization, or the early extended reionization suggested by WMAP (Spergel et al. 2003). For illustration, we show on the lower panel of Figure B10 the filtering mass as a function of redshift for two choices of the reionization redshift. The top panel shows the filtering circular velocity and the corresponding values of the maximum velocity V_m and virial temperature T_{vir} .

Gnedin (2000) provided the following expression for the amount of cold gas left in the halo of mass M :

$$f_g(M, z) = \frac{f_b}{[1 + 0.26M_F(z)/M]^3}, \quad (\text{B3})$$

where $f_b \approx 0.14$ is the universal baryon fraction. In § 6 we use this fraction of cold gas to model the star formation history of the satellite galaxies. To account for the inefficiency of atomic gas cooling at $T < 10^4$ K, we apply equation (B3) substituting for M_F the maximum of $M_F(z)$ or M_4 , the halo mass corresponding to $T_{\text{vir}} = 10^4$ K.